International Journal of Heat and Mass Transfer 146 (2020) 118900

Contents lists available at ScienceDirect

International Journal of Heat and Mass Transfer

journal homepage: www.elsevier.com/locate/ijhmt

An experimental investigation on the dynamic ice accretion and unsteady heat transfer over an airfoil surface with embedded initial ice roughness

Yang Liu [a,b], Kai Zhang [a], Wei Tian [a,c], Hui Hu [a,*]

[a] Department of Aerospace Engineering, Iowa State University, Ames, IA 50011, USA
[b] Department of Engineering, East Carolina University, Greenville, NC 27858, USA
[c] School of Aeronautics and Astronautics, Shanghai Jiao Tong University, Shanghai 200240, China

ARTICLE INFO

Article history:
Received 18 August 2019
Received in revised form 11 October 2019
Accepted 14 October 2019
Available online 22 October 2019

Keywords:
Aircraft icing phenomena
Unsteady heat transfer
Ice accretion process
IR thermal imaging

ABSTRACT

In the present study, a comprehensive experimental study was conducted to evaluate the effects of initial ice roughness formed around the leading-edge of an airfoil model on the dynamic ice accretion and unsteady heat transfer processes over the airfoil surface. The experimental study was performed in the Icing Research Tunnel at Iowa State University, Two airfoil models with the same airfoil shape were manufactured by using a rapid protype machine for a comparative study, i.e., one test model was designed to have embedded initial ice roughness around the airfoil leading-edge and the other model having smooth airfoil leading-edge as the comparison baseline. During the experiments, while a high-speed imaging system was used to record the early-stage icing morphologies over the airfoil surfaces with and without the initial leading-edge roughness, an infrared (IR) thermal imaging system was also utilized to map the corresponding surface temperature distributions over the airfoil surfaces to quantify the unsteady heat transfer and dynamic icing, i.e., phase changing, processes under different test conditions. It was found that, the initial ice roughness formed around the airfoil leading-edge would affect the characteristics of local airflow, impingement of supercooled water droplets, collection and transport of impacted water mass, unsteady heat transfer and subsequent ice accretion processes dramatically. The initial ice roughness formed around the airfoil leading-edge would redistribute the impacted water mass, with more impacted water mass being captured and frozen over the roughness region. In addition, the initial ice roughness was also found to produce span-wise-alternating low- and high-momentum pathways (LMPs and HMPs, respectively), which can significantly affect the convective heat transfer and subsequent ice accretion processes over the airfoil surface.

1. Introduction

Aircraft icing has been recognized as a big threat to flight safety for several decades [1]. The flight performance of an aircraft encountering icing clouds can be significantly contaminated by the ice layers accumulated on critical surfaces [2]. Ice accretions could negatively affect the aerodynamic performance of aircraft by reducing stall margin, increasing drag, and decreasing lift [3]. It is documented that more than 1200 accidents and incidents occurred in the US in the past a few decades [4,5]. Considerable amounts of the accidents/incidents were related to in-flight ice accretion on wings, fuselage or control surfaces of aircraft. While many anti-/de-icing techniques have been developed to mitigate ice accretion on aircraft [6–9], the in-flight icing is still a severe weather hazard to flight safety. The in-flight ice accretion is highly dependent on weather conditions, e.g., cloud liquid water content (LWC), atmosphere temperature, and cloud droplet median volumetric diameter (MVD). Various ice shapes have been observed under different icing cloud conditions [10,11]. In the past years, many efforts have been made to characterize the effects of LWC, air temperature and velocity, and droplet size on ice shape formations [2,3,12]. While clouds with low LWC and small droplets at cold temperatures (typically below −10 °C) tend to produce ice shapes with rough, milky white appearance conforming to aircraft surfaces, i.e., rime ice, some irregular ice horns with clear, smooth, and dense appearance, i.e., glaze ice, may form and extend into the oncoming flows under other cloud conditions with high LWC and large droplets at temperatures just below the freezing point [13].

* Corresponding author.
E-mail address: huhui@iastate.edu (H. Hu).

https://doi.org/10.1016/j.ijheatmasstransfer.2019.118900
0017-9310/

Heat transfer is one of the most essential mechanisms that control the ice accretion on aircraft [14]. Ice forms when the latent heat of fusion in the impinged water mass is removed by heat transfer. If the heat transfer is sufficiently fast to remove all of the latent heat of fusion in the impinged water droplets, they would freeze immediately upon impacting on the aircraft surfaces. If not, however, only a portion of the impinged water mass would be frozen upon impact, with the remaining being transported downstream and frozen over a larger area. Many experimental studies, either in-flight or ground wind tunnel test, have been conducted to evaluate the heat transfer in aircraft icing [15,16]. It has been revealed that the heat transfer during icing processes is significantly affected by the roughness elements formed in the initial stage of ice accretion. Further studies showed that the initial ice roughness is significant because it couples the fluid flow, droplet impingement, and heat transfer processes [17,18]. The initial ice roughness essentially induces higher turbulence in the airflow, and accelerate the convective heat transfer from the surfaces to freestream [19]. There are multiple heat transfer mechanisms occurring on the airfoil/ice surfaces during ice accretion [20,21], among which, convective heat transfer is considered to be predominant in aircraft icing [16,22]. Since the initial ice roughness is closely coupled with the local flow field and convective heat transfer, even a slight change in roughness characteristics (element size, element spacing, etc.) could essentially impact the convective heat transfer, and hence, change the amount and rate of ice accretion [23].

During the past years, some ice accretion prediction codes have been developed to simulate icing process from water droplet trajectory calculations to ice growth on aircraft surfaces. However, these codes are limited in their capabilities in predicting ice accretion especially in glaze conditions. An important reason for that is the use of simplified ice roughness models. For example, in the LEWICE code [1], the ice roughness height is estimated based on the sand-grain equivalent model. Convective heat transfer is then determined by coupling with the ice roughness height estimation [24]. This simplification could essentially affect the ice accretion shape and size because the sand-grain roughness is different from the actual ice roughness formed in in-flight icing conditions [25]. Based on the comparison of the ice shapes generated in the icing experiments and that from the LEWICE simulation, it was found that the predicted ice shapes did not match well with the experimental results. The comparison, consequently, presented a poor agreement of the convective heat transfer coefficients [26].

Many experimental studies have been conducted to evaluate the effects of the roughness elements on the local convective heat transfer and boundary layer development. However, due to the difficulties in characterizing the initial ice roughness, most of these studies have focused on the effects of the non-realistic ice roughness, or simplistically distributed roughness [27–29]. Although these simulated roughness elements can be easily generated and manufactured, they may not reflect the irregularity and broad range of topographical scales of practical roughness [30]. The unique ice surface features formed in actual in-flight icing conditions would not be captured by the ordered arrays of discrete roughness elements. The use of these non-realistic ice roughness has created biases in convective heat transfer coefficients in comparison to those with the realistic distributions of roughness elements [31]. Thus, assessing the impact of realistic ice roughness on the heat transfer and further ice accretion is of great importance to improve our understanding of the nonlinear icing processes on aircraft.

Over the years, several techniques have been developed to create realistic ice roughness distributions [32]. One recent example is the Lagrangian droplet simulator, which can be used to generate realistic ice roughness distributions [23,32]. The generated roughness is a bead distribution with random spreading and diameters. This approach enables the characterization of boundary layer development and convective heat transfer from surfaces exhibiting such kind of roughness distributions [23]. Since the actual ice roughness generated in real icing conditions could be of various shapes and sizes, another approach employing cast surfaces of real icing models was developed [22] in order to characterize the boundary layer flow and local heat transfer in these situations. While the three-dimensional ice roughness features can be captured using the mold and casting method, this approach is time consuming in operation, and the cost can be significant [33]. In recent years, laser-based and other optical scanning methods have been developed to accomplish three-dimension, i.e., 3D, digitization of ice accretion [34,35], which are capable to accurately record and reproduce the details of ice roughness features. The advancement of the 3D scanning techniques enables the acquisition of realistic ice roughness data during the early stage of aircraft icing. With such realistic ice roughness data, a series of icing experiments were conducted in the present study to reveal the impacts of these initial ice roughness on the dynamic ice accretion and unsteady heat transfer processes over aircraft wing surfaces. To the best knowledge of the authors, this is the first effort of its kind to quantitatively evaluate the effects of initial ice roughness (with realistic shapes and distributions) in aircraft icing phenomena.

In the present study, two airfoil models with the same airfoil shape, i.e., one model with embedded initial ice roughness around the airfoil leading-edge and the other model with smooth airfoil leading-edge as the comparison baseline, were manufactured by using a rapid protype machine, i.e., 3D printed. The experimental study was performed in the Icing Research Tunnel at Iowa State University, i.e., ISU-IRT. While a high-speed imaging system was used to record the dynamic ice accretion over the airfoil surfaces with and without the initial ice roughness, an infrared (IR) thermal imaging system was also utilized to map the corresponding surface temperature distributions over the airfoil surfaces simultaneously to quantify the unsteady heat transfer and phase changing processes. Such measurements provide insight into the droplet collection distribution and unsteady heat transfer processes with and without the presence of initial ice roughness during the different icing conditions.

2. Test model used in the present study

The two airfoil models used in the present study were designed to have the same NACA 23012 airfoil shape, and were made of a hard-plastic material and manufactured by using a rapid prototyping machine, i.e., 3-D printing, that builds 3-D models layer-by-layer with a resolution of about 25 μm. While one test model was designed to have smooth leading-edge as the comparison baseline, the second model was designed to have embedded realistic initial ice roughness around the airfoil leading-edge. The initial ice roughness was formed under a typical in-flight icing condition, i.e., wind speed of $U_\infty = 102.9$ m/s; LWC = 0.75 g/m^3; MVD = 15 μm, and airflow temperature of $T_\infty = -2.2$ °C, with a icing duration of 30 s, by performing an icing experiment in the Icing Research Tunnel (IRT) at NASA's Glenn Research Center [33]. The iced airfoil model was then 3-D scanned using a 3D laser scanning system. The point cloud data file generated by using the 3-D laser scanning system was used as the input file for designing the airfoil model with realistic ice roughness used in the present study. The construction of the solid airfoil model from the point cloud data is a typical reverse engineering project. The point cloud file was imported into a 3D CAD software (CATIA-V5-R20 in this study) as shown in Fig. 1(a). The imported point cloud was then manipulated, i.e., points filter, local and global points activate

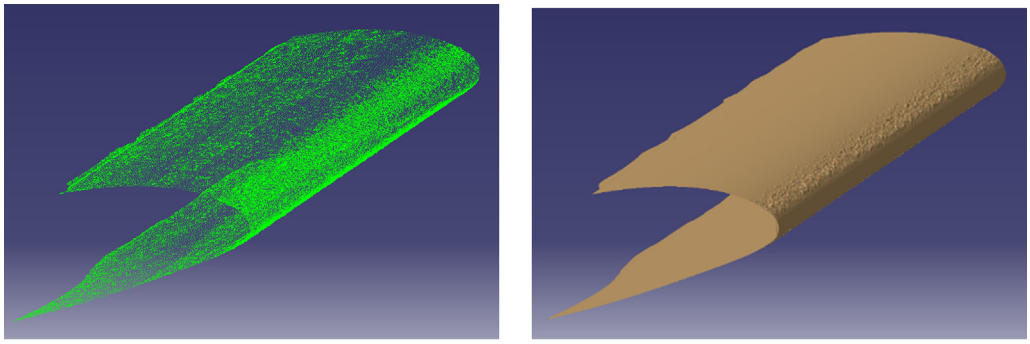

(a) (b)

Fig. 1. (a) Point cloud of the 3D scanned NACA 23012 airfoil with initial ice roughness; (b) Mesh surface of the airfoil containing ice roughness features.

and remove, to generate a mesh surface containing the ice roughness features as can be seen in Fig. 1(b). The mesh surface was further treated by filling holes, flipping edges, and cleaning non-manifold meshes to create the airfoil surface with realistic ice roughness. Finally, the faces and solid body were generated by using the Quick Surface Reconstruction (QSR) module in the CAD software. Fig. 2 shows the zoom-in of the leading-edge ice roughness reconstructed in the present study. It can be clearly seen that, while the roughness elements are of various shapes and sizes and randomly distributed, the stagnation region appears to be smooth which is consistent with the previous studies [36].

By comparing the ice roughened airfoil model and the original smooth airfoil model, the root-mean-square roughness height for the rough surface can be calculated following the work by McClain et al. [32,37,38]:

$$R_q = \left[\frac{1}{N}\sum_{i=1}^{N}\left(y_i - \bar{y}_i\right)^2\right]^{\frac{1}{2}} \quad (1)$$

where N is the number of points at a specific surface distance, $\left(y_i - \bar{y}_i\right)$ is the local height difference between the ice-roughened surface and the smooth surface. Thus, the 99% roughness maximum height (RMH) based on a Gaussian distribution can be calculated using three times the root-mean-square roughness height [37]:

$$RMH = 3R_q = 3\left[\frac{1}{N}\sum_{i=1}^{N}\left(y_i - \bar{y}_i\right)^2\right]^{\frac{1}{2}} \quad (2)$$

Fig. 3 shows the ice roughness distribution over the airfoil model. It should be noted that the roughness distribution agrees well with that extracted using a Self-Organizing-Map approach by McClain [37]. As can be seen clearly in Fig. 3, there is a significant difference between the roughness height on the suction side and that on the pressure side of the airfoil model, as separated by the "smooth" stagnation region. It is suggested that such difference is essentially caused by the asymmetrical profile of the NACA 23012 airfoil, which influences the water collection efficiency and heat transfer properties.

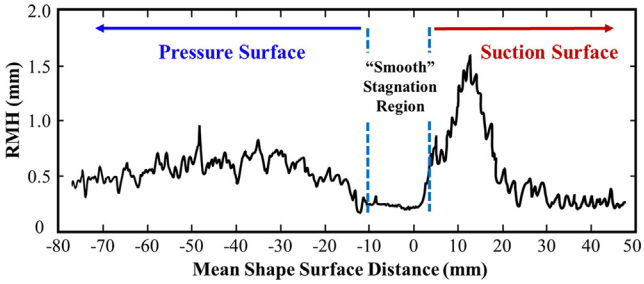

Fig. 3. Roughness distribution over the NACA 23012 airfoil model.

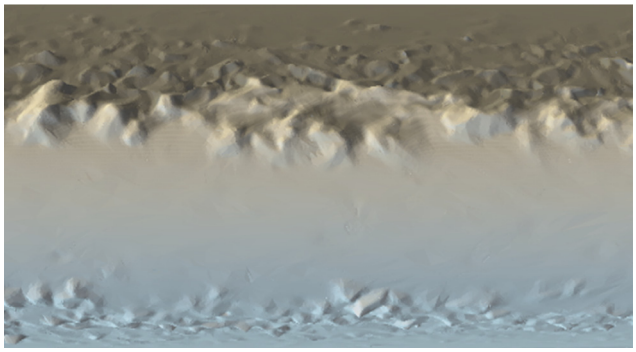

Fig. 2. Zoom-in of the leading-edge ice roughness on the NACA 23012 airfoil model.

3. Experimental setup for the icing experiments

As shown schematically in Fig. 4, ISU-IRT is a multifunctional icing research tunnel with a test section of 2.0 m in length × 0.4 m in width × 0.4 m in height with four sidewalls being optically transparent. It has a capacity of generating a maximum wind speed of 60 m/s and an airflow temperature down to −25 °C. An array of 8 pneumatic atomizer/spray nozzles are installed at the entrance of the contraction section of the icing tunnel to inject micro-sized water droplets (10–100 μm in size with MVD ≈ 20 μm) into the airflow. By manipulating the water flow rate through the spray nozzles, the liquid water content (LWC) in the ISU-IRT could be adjusted, i.e., *LWC* ranging from 0.1 g/m^3 to 5.0 g/m^3. In summary, ISU-IRT can be used to simulate atmospheric icing phenomena over a range of icing conditions, i.e., from dry *rime* to extremely wet *glaze* ice conditions.

Supported by a stainless-steel rod, the airfoil model was mounted at its quarter-chord and oriented horizontally across the middle of the test section. In the present study, two typical icing conditions, i.e., glaze and rime, were generated in the ISU-IRT as described in 14 CFR Part 25 Appendix C, i.e., at the free-stream air velocity of U_∞ = 40 m/s, *LWC* = 1.0 g/m^3, and airflow temperature of T_∞ = −5 °C and −15 °C, respectively. The angle of attack (α) of the airfoil model was set at $\alpha = 2°$ in accordance with the previous studies [33,37].

During the experiments, the dynamic ice accretion process over the airfoil surface was recorded by using a high-speed camera (PCO Tech, Dimax) with a 60 mm lens (Nikon, 60 mm Nikkor f/2.8)

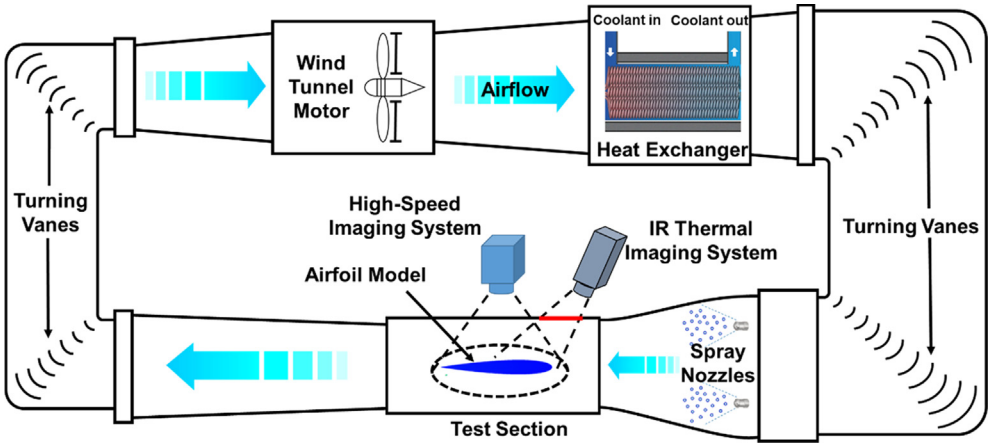

Fig. 4. Schematic of the ISU-IRT and tested airfoil model used in the present study.

installed at 500 mm above the airfoil model. The camera was positioned approximately normal to the airfoil chord, with a measurement window size of 210 mm × 210 mm and a spatial resolution of 9.5 pixels/mm. An in-situ calibration procedure as suggested by Soloff et al. [39] was performed to dewarp the captured images before extracting physical features. Each test trial consisted of 3000 images acquired at a frame rate of 50 Hz. A pair of 100 W Studio-LED light Units (RPS Studio Light, Model RS-5610 and RS-5620) were used in the present study to provide low-flicker illumination for the image acquisition. The imaging system was calibrated by placing a calibration target consisting of a grid of dots aligned in the plane defined by the airfoil span and chord and computing a planar homography using the direct linear transform method, thus mapping the pixel coordinates to real-space coordinates projected onto the airfoil plane (with an uncertainty of ±0.1 mm in location definition). It should be noted that, after the icing images were acquired, a series image processing, i.e., noise removal, contrast adjustment, and intensity normalization, were performed to provide high-quality images for analysis. As shown in Fig. 4, an infrared (IR) thermal imaging camera (FLIR A615) was also used to map the surface temperature of the ice accreting airfoil surface. The IR camera was mounted at ~300 mm above the airfoil model with the measurement window size of 110 mm × 90 mm and a corresponding spatial resolution of 5.3 pixels/mm. Radiation from the ice accreting airfoil surface passes through an infrared window (FLIR IR Window-IRW-4C with optic material of Calcium Fluoride) before reaching to the IR camera. A calibration of the material emissivity is performed for the IR thermal imaging [40]. Table 1 gives the IR emissivity coefficients of the materials relevant to the present study, i.e., surface of the airfoil model, ice, and liquid water, respectively. Each test trial consisted of 15,000 IR images acquired at a frame rate of 50 Hz. An in-situ calibration was also performed to validate the IR thermal imaging results by establishing a relationship between the measured count number from the IR camera and the temperature acquired by using thermocouples (T-type thermocouple with an accuracy of ±0.5 °C). The measurement uncertainty for the IR camera was found to be less than 0.2 °C. The high-speed video camera and the IR camera were connected to a digital delay generator (DDG, Berkeley Nucleonics, model 575) that synchronized the timing between the two systems.

Table 1
Emissivity of the materials pertinent to the test model used in the present study.

Materials	Emissivity
Surface of the airfoil/wing model (Enamel coated)	0.960
Ice	0.965
Water	0.950–0.963

4. Results and discussion

4.1. Surface morphology of the ice accreting airfoil model with and without the initial roughness

It is known that the early-stage water collection and ice accretion have a significant effect on the final ice shape growth and extension [16,19]. When ice roughness forms around the leading-edge of an aircraft wing in the early-stage of ice accretion, the water collection efficiency, boundary layer airflow, and heat transfer would be rapidly changed [41]. In order to evaluate the instantaneous effects of such initial ice roughness on the water collection and icing morphology, the present study focused on the starting period of the ice accretion process, i.e., the first 5 s of ice accretion. The airfoil models (with and without the initial leading-edge roughness) were tested under two typical icing conditions, i.e., rime and glaze. Multiple trials were conducted under each test condition to examine the repeatability of the experiment. It was found that while discrepancies were observed in the icing morphology in terms of icing rivulet spaces and locations (which is suggested to be caused by the uncertain disturbs in upstream), the main features of the ice accretion were basically the same.

Fig. 5 shows the typical snapshots of ice accretion over the two airfoil model surfaces under the icing condition of U_∞ = 40 m/s, T_∞ = −15 °C, and LWC = 1.0 g/m^3. It is clearly seen that, when the super-cooled water droplets impinged onto the smooth leading-edge, i.e., Fig. 5(a)–(e), a thin ice film was quickly formed around the leading-edge, exhibiting similar characteristics as that described in the previous study [42]. In addition to the formation of the ice film, sparse ice roughness was also observed to grow at the edge of the ice film. Since the airflow temperature is freezing cold in this case, the impinged water mass were found to freeze immediately upon impacting on the airfoil surface. There was no surface water run-back or downstream icing being observed under this condition. It should be noted that, along with the extension of the ice film, a distinct straight boundary was also observed between the smooth ice film and the rough spots region as indicated by the blue dashed lines given in Fig. 5(b)–(e). Since the ice accretion process in this case is a typical rime icing, the distribution of ice accretion is solely determined by the water collection distribution [36]. Based on the surface morphology of the ice accreting airfoil model in Fig. 5(e), it is revealed that while the

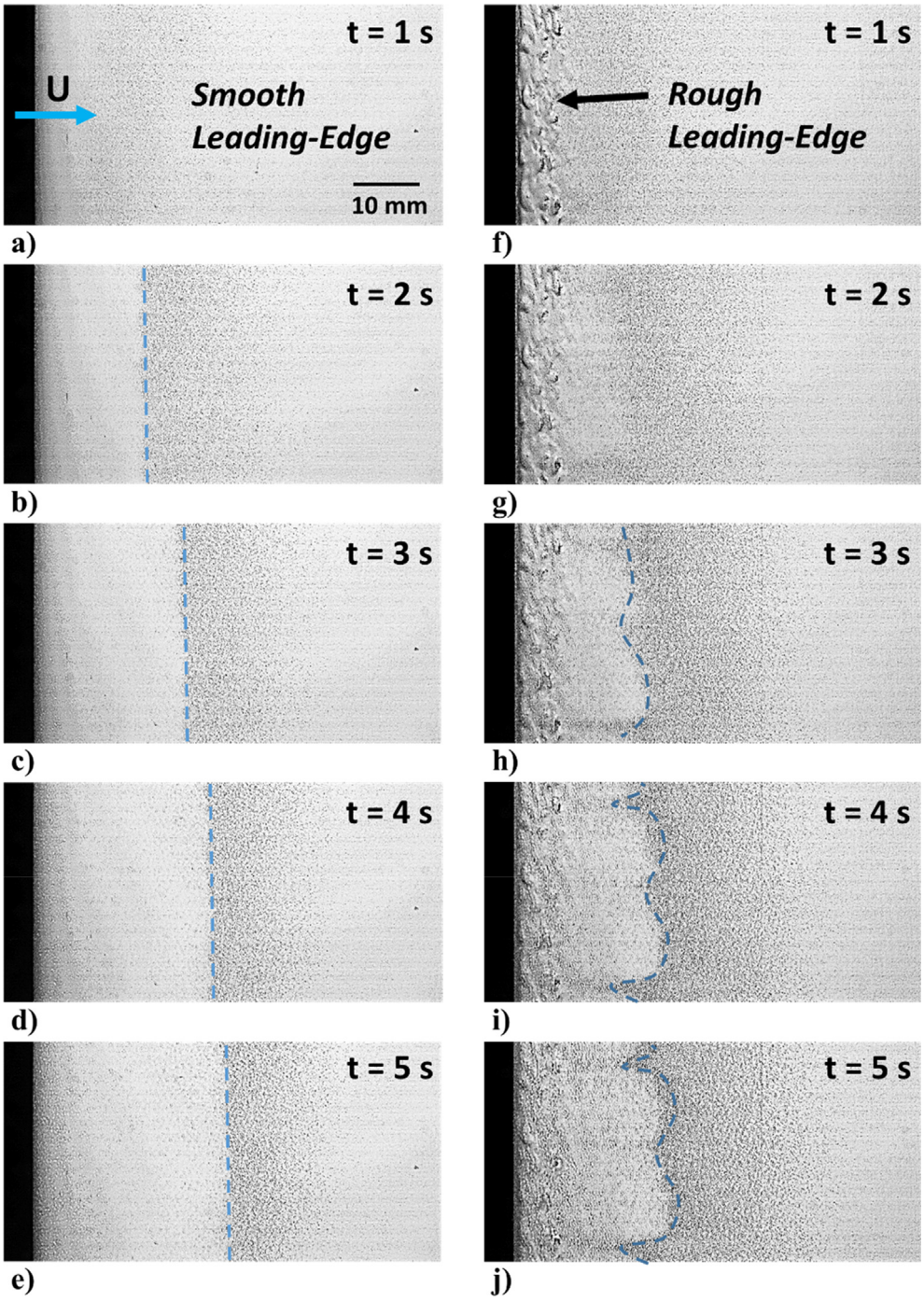

Fig. 5. Snapshots of early-stage ice accretion process on the airfoil with smooth leading-edge ((a)–(e)) and initial leading-edge roughness ((f)–(j)) under the test condition of U_∞ = 40 m/s, LWC = 1.0 g/m^3, and T_∞ = −15 °C.

ice accretion is uniformly distributed along spanwise, the ice thickness appears to be decreasing at further downstream, which agrees well with the previous study [43].

For the icing morphology over the airfoil surface with the initial leading-edge roughness, it is found that a finger-like boundary was formed between the ice film region and the rough spots region as shown in Fig. 5(h)–(j). As the super-cooled water droplets impinged onto the airfoil surface, due to the blockage at the elevated elements and the trap at the recessed spots, the water collection distribution was significantly altered. Along with the redistribution of the water collection, the amount of ice accretion was also redistributed. Such variation of the initial water collection and ice accretion is suggested to have a great impact on the subsequent ice accretion processes.

Fig. 6 shows the typical snapshots of ice accretion over the two airfoil model surfaces under the glaze icing condition, i.e., U_∞ = 40 m/s, T_∞ = −5 °C, and LWC = 1.0 g/m^3. When the super-cooled water droplets impinged onto the airfoil model with the smooth leading-edge, i.e., Fig. 6(a)–(e), due to the relatively warm airflow temperature, the heat transfer was not sufficient to instantly remove all the latent heat of fusion in the collected water. As a result, only partial of the impinged water froze upon impact, with

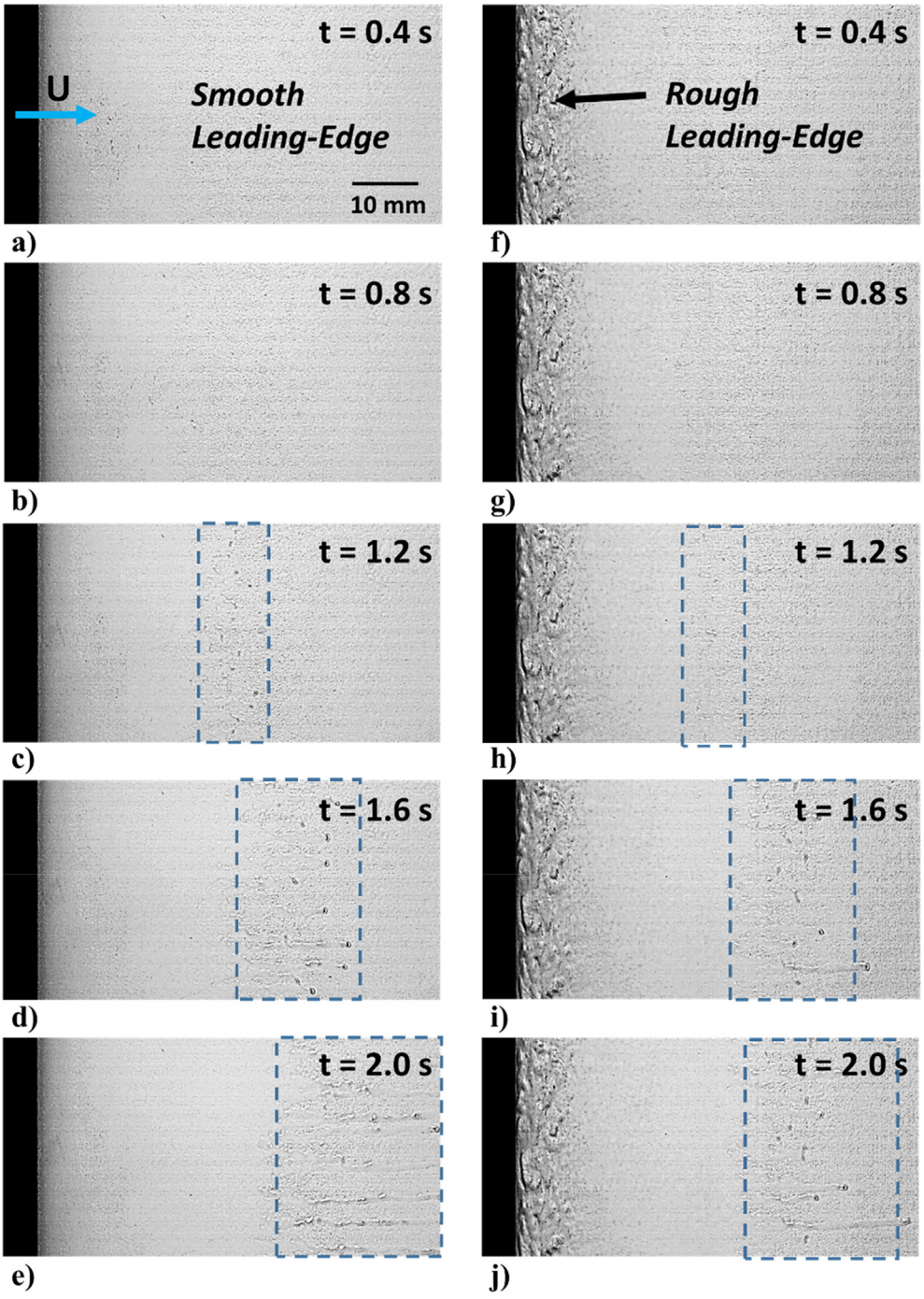

Fig. 6. Snapshots of early-stage ice accretion process on the airfoil with smooth leading edge ((a)–(e)) and initial leading-edge roughness ((f)–(j)) under the test condition of U_∞ = 40 m/s, LWC = 1.0 g/m^3, and T_∞ = −5°C.

the remaining being transported downstream as driven by the boundary layer airflow. Thus, a smooth water/ice film was found to be formed around the airfoil leading edge. As more water droplets impinged on the surface, run-back rivulets were found to be formed as can be seen in Fig. 6(c)–(e).

For the ice accretion over the airfoil model with the initial leading-edge roughness, it is found that, though the leading-edge roughness redistributed the water collection, a similar water/ice run-back behavior was observed as can be seen in Fig. 6(f)–(j). Since the heat transfer under this test condition was not sufficient to remove all the latent heat of fusion in the collected water, the unfrozen water was found to run back and flush over the roughness elements. The leading-edge roughness was found to trap the surface water run-back and decelerates the water/ice film formation. In addition to the redistribution of water collection, the roughness elements are also suggested to change the boundary layer airflow, and enhance the heat convection at specific regions, which will be discussed in following sections.

4.2. Temperature mapping of the ice accreting airfoil model with and without the initial roughness

In order to further evaluate the effects of the initial ice roughness on the water collection, heat transfer, and water/ice transport

process, the transient surface temperature distributions over the ice accreting airfoil models were also quantitatively measured. Fig. 7 shows the time-evolution of the measured surface temperature distribution over the airfoil models during the early-stage ice accretion processes under the test condition of U_∞ = 40 m/s, T_∞ = −15 °C, and LWC = 1.0 g/m^3. Since the amount of ice accretion is linearly related to the amount of the latent heat release during the solidification process [16], the temperature maps derived in Fig. 7 can be used to quantitatively describe the ice accretion distribution over the different airfoil surfaces. For the ice accretion over the airfoil model with the smooth leading-edge, i.e., Fig. 7 (a)–(e), it is found that as the super-cooled water droplets impinged onto the airfoil surface, an ice film was quickly formed and extended downstream. It should be noted that, the temperature distribution is uniform along the spanwise direction, indicating that the amount of water collection and the subsequent ice accretion are uniformly distributed along spanwise over the airfoil model. It is also found that, as more water droplets impinged onto the airfoil surface, along with the extension of ice film, an evident temperature gradient appeared along the chordwise direction, which corresponds to the water collection and ice accretion distribution [16,43].

For the ice accretion over the airfoil model with the initial leading-edge roughness, i.e., Fig. 7(f)–(j), it is found that the realistic roughness elements essentially changed the water impingement distribution. Based on the temperature map at the very beginning of water collection, i.e., Fig. 7(f)–(g), it can seen clearly that there is an evident variation of the water collection in both span- and chord-wise directions. As more water droplets impinged onto the airfoil surface, an ice film was found to be formed over the roughness elements. It is found that along with the extension of the ice film, jagged boundaries appeared as indicated by the temperature gradient in Fig. 7(h)–(j). It is suggested that such alternative "crests" and "troughs" appeared at the temperature boundaries are essentially caused by the greatly altered water collection distribution induced by the roughness elements.

Fig. 8 shows the time-evolution of the measured surface temperature distributions over the airfoil models with and without the initial roughness under the test condition of U_∞ = 40 m/s, T_∞ = −5 °C, and LWC = 1.0 g/m^3. As described above, the ice accretion under this test condition is a typical glaze ice accretion with evident surface water/ice run-back over the airfoil model surfaces. For the ice accretion over the airfoil model with smooth leading-edge, i.e., Fig. 8(a)–(e), it is clearly seen that, as the water droplets impinged on the smooth leading-edge, the temperature map appeared to be not uniform as shown in Fig. 8(a). Since the heat convection is not adequate to remove all the latent heat of fusion

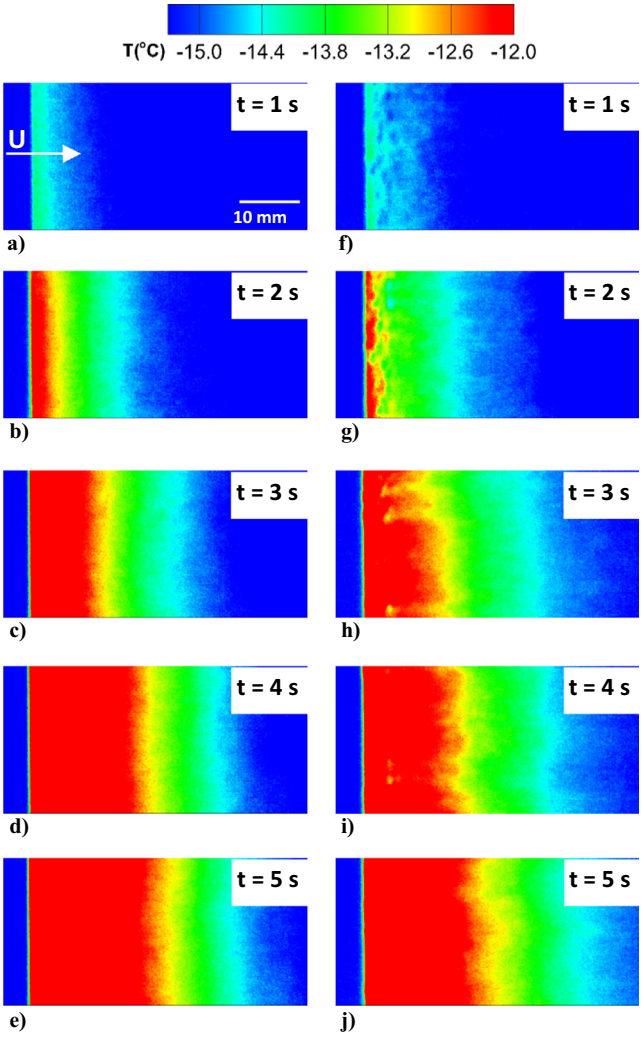

Fig. 7. Time-evolution of the measured surface temperature distribution over the airfoil models during the early-stage ice accretion processes under the test condition of U_∞ = 40 m/s, T_∞ = −15 °C, and LWC = 1.0 g/m^3. (a)–(e): with the smooth leading edge; (f)–(j): with the rough leading edge.

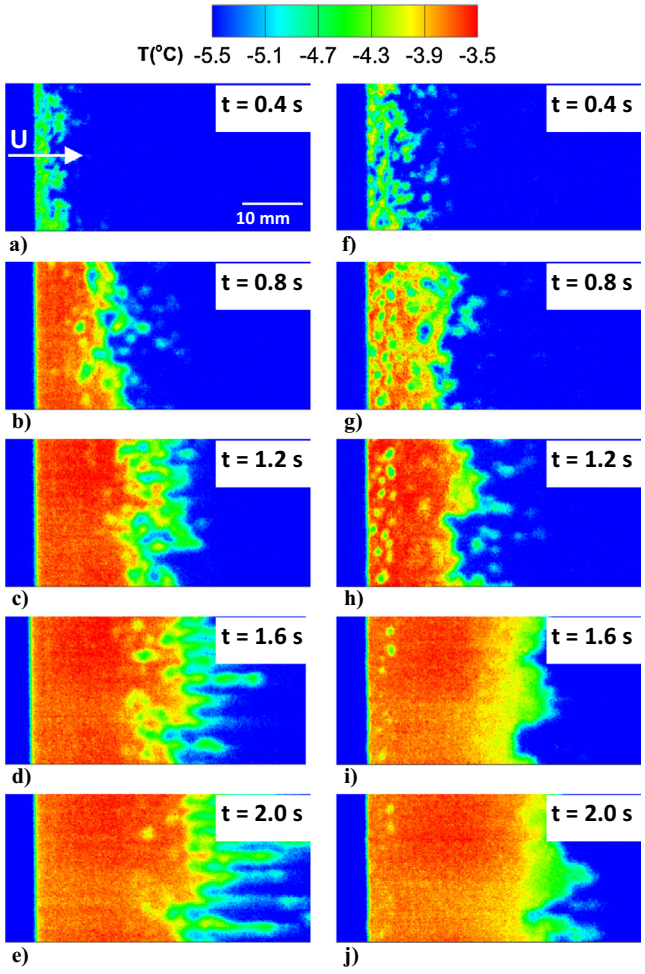

Fig. 8. Time-evolution of the measured surface temperature distribution over the airfoil models during the early-stage ice accretion processes under the test condition of U_∞ = 40 m/s, T_∞ = −5 °C, and LWC = 1.0 g/m^3. (a)–(e): with the smooth leading edge; (f)–(j): with the rough leading edge.

in the impinged water, the impinged water droplets would experience a deform and splash process before freezing. Due to the variation of droplet impinging behaviors at the different locations, the water deposition/ice accretion were found to be disorderly distributed as indicated by the temperature distribution in Fig. 8(a). As more and more water droplets impinged onto the airfoil surface, a water/ice film was found to be formed and transported downstream. During this process, water/ice beads and rivulets were found to be formed due to the instability of the surface water transport [44–46] as can be seen in Fig. 8(b)–(e). The temperature maps indicate that, while partial of the impinged water was frozen into ice film around the leading-edge, a large amount of the water was frozen into the rivulets-shaped ice as it transported downstream.

For the ice accretion over the airfoil model with the initial leading-edge roughness, i.e., Fig. 8(f)–(j), due to the existence of the initial roughness elements, the impinging behaviors of the water droplets were found to be even more complicated. While the roughness altered the water collection distribution by blocking and trapping water mass at the elevated elements and the recessed spots, the impinged water mass was found to be further redistributed during the run-back process as shown in Fig. 8(f)–(h). As more and more water droplets impinged onto the airfoil surface, the water/ice flushed over the roughness elements, and transported downstream. The roughness elements trapped the water film flow and decelerated the water/ice transport. Due to the redirection and deceleration of the roughness elements, the run-back water/ice was found to have fewer beads/rivulets formation as compared with that over the airfoil model with smooth leading-edge.

4.3. Effects of initial ice roughness on water collection distribution over the ice accreting airfoil model

As described above, the initial ice roughness would significantly affect the droplet impinging behaviors and water mass distribution. Based on the previous study of Liu and Hu [16], it was found that the water collection efficiency is proportional to the surface temperature increment during the ice accretion process under rime icing conditions. Thus, the relative water collection efficiency around the airfoil leading-edge can be estimated directly based on the measured surface temperature distributions, i.e., $s\overline{\beta}_i - = \beta_i / \beta_0 = \Delta T_i / \Delta T_0$, where is the relative water collection efficiency, β_i is the local water collection efficiency, β_0 is the water collection efficiency at the stagnation point, ΔT_i is the local temperature increment, and ΔT_0 is the temperature increment at the stagnation point of the airfoil model. In the present study, the leading-edge temperature distributions at the very beginning of ice accretion (t = 0.5 s) under the rime condition, i.e., U_∞ = 40 m/s, T_∞ = −15 °C, and LWC = 1.0 g/m^3, were used to elucidate the effects of the initial ice roughness on the water collection process.

Fig. 9 shows the leading-edge temperature distributions and span-averaged temperature distributions over the smooth and the rough leading-edge at the very beginning of ice accretion (t = 0.5 s) under the test condition of U_∞ = 40 m/s; LWC = 1.0 g/m^3; and T_∞ = −15 °C. It can be seen clearly that, while the surface temperature over the smooth leading-edge is uniformly distributed along the spanwise direction, the temperature distribution over the rough leading-edge appears to be much more irregular. By averaging the chordwise temperature increment distribution along spanwise, the overall temperature increment distribution in chordwise can be acquired as shown in Fig. 9. It is found that for both models, the maximum temperature increment, i.e., maximum water collection, occurs at the stagnation point as indicated by the black dashed lines in Fig. 9. The water collection efficiency gradually decreases at downstream locations as indicated by the decreasing temperature increment along the chordwise direction. This distribution is in accordance with the water collection efficiency distribution derived in the previous studies [47]. However, for the airfoil model with the initial roughness, it is found that while the overall chordwise water collection distribution follows a similar trend as that of the smooth model, a greater temperature drop, i.e., indicating a quick reduction of water collection efficiency, occurs right after the stagnation point. It is suggested that the roughness elements tend to block and capture more water droplets, resulting in a smaller and more concentrated water collection area around the airfoil leading-edge.

In order to further evaluate the effects of initial ice roughness on the water collection distribution, the spanwise temperature increment distribution at three chordwise locations (X/C = 0.002, 0.010, and 0.020) were also extracted for both airfoil models with and without the initial roughness as shown in Fig. 10. It is seen clearly that, the spanwise temperature increment distribution over the smooth leading edge is almost constant with only small variations, indicating a uniform water collection along the spanwise direction. For the airfoil model with the initial roughness elements, however, the surface temperature distribution appears to be in an irregular jagged profile, indicating a significant fluctuation of water collection along the spanwise direction. The existence of the leading-edge roughness elements essentially breaks the uniformity of the spanwise water collection distribution, and the variation of the local water collection is suggested to be closely related to the intense span-wise gradients in topographical height.

4.4. Effects of initial ice roughness on convective heat transfer over the ice accreting airfoil model

The above sections have revealed that the initial ice roughness could essentially redistribute the impinged water mass. More importantly, the roughness elements are also suggested to have a significant impact on the boundary layer airflow and convective heat transfer [48]. In order to better understand the effects of initial ice roughness on the heat transfer and the subsequent ice accretion processes, the high-speed video snapshots and the corresponding IR images of the ice accreting airfoil models (with and without the initial leading-edge roughness) taken after a short period of ice accretion, i.e., t = 10 s, under the test condition of U_∞ = 40 m/s; LWC = 1.0 g/m^3; and T_∞ = −15 °C, were selected for a more insightful analysis in this section.

Fig. 11 shows the snapshots of the surface icing morphologies of the airfoil models with and without the initial leading-edge roughness. It can be seen clearly that, when ice accretes over the airfoil model with the smooth leading-edge, there is a distinct straight line boundary between the smooth ice film and the rough spots regions as shown in Fig. 11(a). The ice accretion uniformly distributes along spanwise. For the airfoil model with the initial leading-edge roughness, however, it is found that the ice accretion appears to form a finger-like boundary between the ice regions as shown in Fig. 11(b). The ice “crests” are identified in numbers as shown in the figure.

It has been revealed that the realistic roughness distribution could induce span-wise-alternating low- and high-momentum pathways (LMPs and HMPs, respectively) separated by streamwise-oriented swirling motions with LMPs embodying intense regions of enhanced turbulence kinetic energy (TKE) [49]. Based on the icing morphologies shown in Fig. 11, it is suggested that there is a similar distribution of LMPs and HMPs over the airfoil model with the initial leading-edge roughness. More ice tends to be accreted along the LMPs due to the encountering vortices and enhanced TKE [49]. Since the surface temperature increment is directly related to the amount of latent heat release during the solidification process, i.e., the amount of ice accretion, more

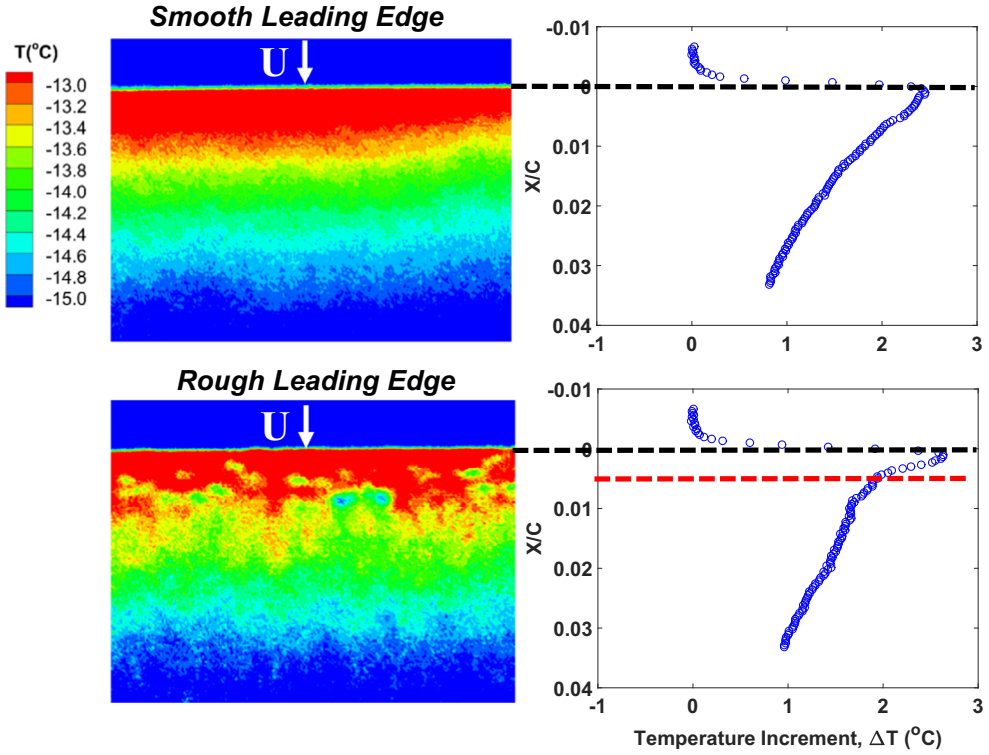

Fig. 9. Leading-edge temperature distribution and span-averaged temperature distribution over the smooth and the rough leading-edge at t = 0.5 s under the test condition of U_∞ = 40 m/s; LWC = 1.0 g/m^3; and T_∞ = −15 °C. X/C is the normalized chordwise location where X is the chordwise coordinate and C is the airfoil chord length.

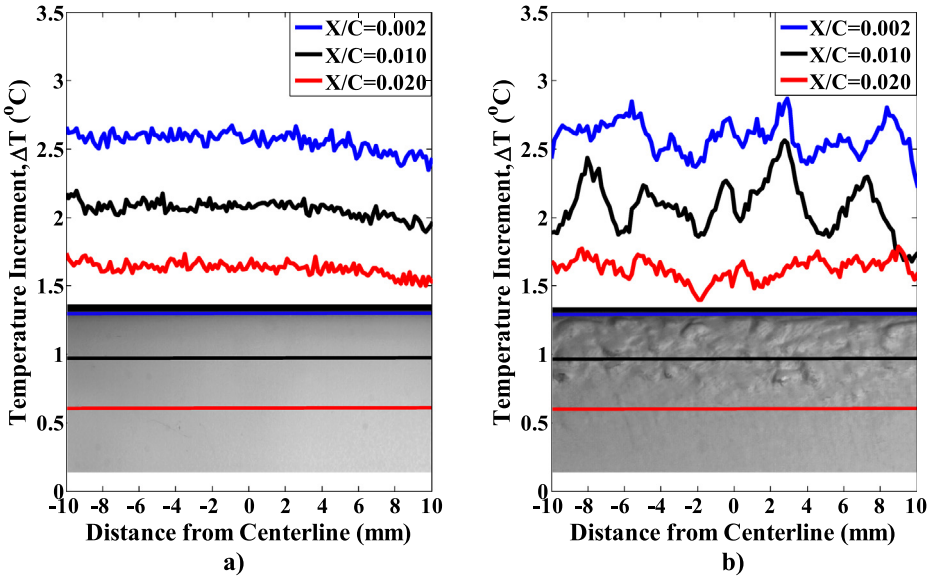

Fig. 10. Span-wise temperature distribution over (a) smooth leading edge, and (b) rough leading edge under the test condition of U_∞ = 40 m/s; LWC = 1.0 g/m^3; and T_∞ = −15 °C.

evidences of the surface icing distribution and the potential LMPs and HMPs distribution are derived based on the temperature distribution given in Fig. 12. It can be seen that, for the ice accretion over the airfoil model with the smooth leading-edge, an obvious temperature gradient exists with distinct straight boundaries as shown in Fig. 12(a). For the airfoil model with the initial leading-edge roughness, however, the surface temperature distribution appears to be in a form with multiple finger-like boundaries between the temperature gradients as shown in Fig. 12(b). Since more ice tends to be accreted along the LMPs induced by realistic roughness [49], a larger temperature increment would be observed in these regions. Thus, an estimation of the LMPs and HMPs distribution is derived as indicated in Fig. 12(b). Since the LMPs has higher TKE, i.e., enhanced convective heat transfer, and tends to capture more ice, such initial ice roughness is suggested to generate a wave-like ice shape, i.e., ice "crest" located along the LMPs, and ice "trough" located along the HMPs, in the subsequent icing process.

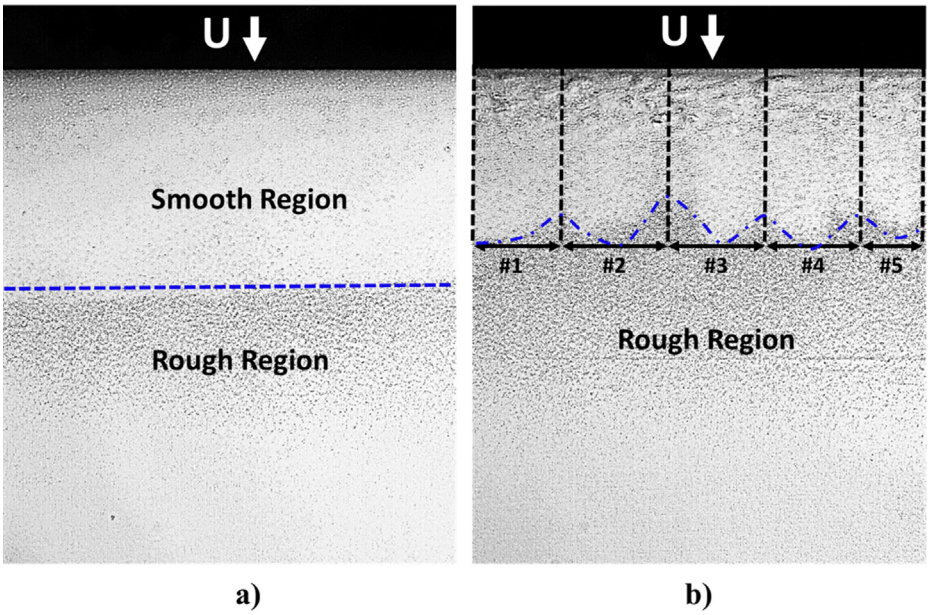

Fig. 11. Ice accretion over (a) smooth leading edge, and (b) rough leading edge under the test condition of U_∞ = 40 m/s; LWC = 1.0 g/m^3; and T_∞ = −15 °C.

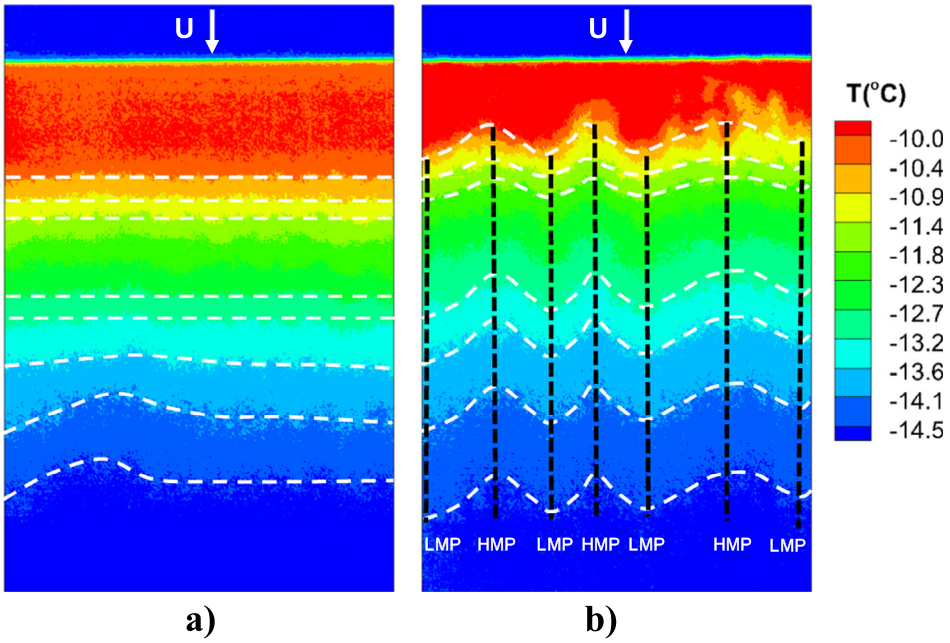

Fig. 12. Temperature mapping over (a) smooth and (b) rough leading edge under test conditions of U = 40 m/s; LWC = 1.0 g/m^3; and T = −15 °C.

5. Conclusion

In the present study, an experimental study was conducted to investigate the effects of initial ice roughness formed around the airfoil leading-edge on the dynamic ice accretion and unsteady heat transfer processes over the airfoil surface. Based on the high-speed imaging and infrared (IR) thermal imaging of the ice accreting airfoil surfaces, it is revealed clearly that, the initial ice roughness accreted around the airofil leading-edge could dramatically change the water collection distribution. The averaged chordwise temperature profiles show that, while the overall chordwise water collection distributions follow a similar trend for both airfoil models with and without the initial leading-edge roughness, the model with the ice roughness elements tends to block and capture more water within the roughness region. The roughness elements essentially break the uniformity of the spanwise water collection distribution, and the variation of the local water collection is suggested to be closely related to the intense span-wise gradients in topographical height.

It was also found that, while the ice accretion on the airfoil model with the smooth leading-edge is uniformly distributed along the spanwise direction with clear temperature gradient in chordwise, the ice accretion on the airfoil model with embbeded initial ice roughness appears to be in a form of multiple finger-like boundaries between the temperature gradients. Distinct “crests” and “trough” in the temperature distribution are suggested to represent the low-momentum pathways and high-momentum pathways, which may produce alternative high and

low heat convection channels and contribute to the variation of ice mass distribution in the subsequent icing process.

Declaration of Competing Interest

The authors declared that there is no conflict of interest.

Acknowledgments

The research work is partially supported by Iowa Energy Center for Wind Turbine Icing Study under the IEC Competitive Grant # 312350 and National Science Foundation (NSF) under award numbers of CMMI-1824840 and CBET-1916380.

References

[1] M.G. Potapczuk, Aircraft Icing Research at NASA Glenn Research Center, J. Aerosp. Eng. 26 (2013) 260–276.
[2] T. Cebeci, F. Kafyeke, Aircraft icing, Annu. Rev. Fluid Mech. 35 (2003) 11–21.
[3] R.W. Gent, N.P. Dart, J.T. Cansdale, Aircraft icing, Philos. Trans. R. Soc. London. Ser. A Math. Phys. Eng. Sci. 358 (2000) 2873–2911.
[4] S.D. Green, A study of US inflight icing accidents and incidents, 1978 to 2002, in: 44th AIAA Aerosp. Sci. Meet. Exhib., Reno, Nevada, 2006.
[5] P. Appiah-Kubi, US Inflight Icing Accidents and Incidents, 2006 to 2010, University of Tennessee, 2011. http://trace.tennessee.edu/utk_gradthes/1055.
[6] X. Meng, H. Hu, C. Li, A.A. Abbasi, J. Cai, H. Hu, Mechanism study of coupled aerodynamic and thermal effects using plasma actuation for anti-icing, Phys. Fluids 31 (2019), https://doi.org/10.1063/1.5086884.
[7] S.G. Pouryoussefi, M. Mirzaei, F. Alinejad, S.M. Pouryoussefi, Experimental investigation of separation bubble control on an iced airfoil using plasma actuator, Appl. Therm. Eng. 100 (2016) 1334–1341, https://doi.org/10.1016/j.applthermaleng.2016.02.133.
[8] Y. Liu, C. Kolbakir, H. Hu, X. Meng, H. Hu, An experimental study on the thermal effects of duty-cycled plasma actuation pertinent to aircraft icing mitigation, Int. J. Heat Mass Transf. 136 (2019) 864–876, https://doi.org/10.1016/J.IJHEATMASSTRANSFER.2019.03.068.
[9] L. Li, Y. Liu, Z. Zhang, H. Hu, Effects of thermal conductivity of airframe substrate on the dynamic ice accretion process pertinent to UAS inflight icing phenomena, Int. J. Heat Mass Transf. 131 (2019) 1184–1195, https://doi.org/10.1016/J.IJHEATMASSTRANSFER.2018.11.132.
[10] J. Shin, T.H. Bond, Results of an icing test on a NACA 0012 airfoil in the NASA Lewis Icing Research Tunnel, in: 30th Aerosp. Sci. Meet. Exhib., American Institute of Aeronautics and Astronautics, Reno, 1992.
[11] M. Vargas, J.-C. Tsao, Time-Sequence Observations of the Formation of Ice Accretions on Swept Wings, in: 46th AIAA Aerosp. Sci. Meet. Exhib., American Institute of Aeronautics and Astronautics, 2008. https://doi.org/10.2514/6.2008-470.
[12] R.J. Hansman, M.S. Kirby, Measurement of ice growth during simulated and natural icing conditions using ultrasonic pulse-echo techniques, J. Aircr. 23 (1986) 492–498.
[13] R.J. Hansman, M.S. Kirby, Comparison of wet and dry growth in artificial and flight icing conditions, J. Thermophys. Heat Transf. 1 (1987) 215–221.
[14] K. Yamaguchi, R.J. Hansman, Heat transfer on accreting ice surfaces, J. Aircr. 29 (1992) 108–113.
[15] P.E. Poinsatte, G.J. Vanfossen, K.J. Dewitt, Convective heat transfer measurements from a NACA 0012 airfoil in flight and in the NASA Lewis Icing Research Tunnel, in: 27th AIAA Aerosp. Sci. Meet., 1989, pp. 8–11.
[16] Y. Liu, H. Hu, An experimental investigation on the unsteady heat transfer process over an ice accreting airfoil surface, Int. J. Heat Mass Transf. 122 (2018) 707–718, https://doi.org/10.1016/j.ijheatmasstransfer.2018.02.023.
[17] N. Dukhan, J. Va G, K. Masiulaniec, K. DeWitt, Convective heat transfer coefficients from various types of ice roughened surfaces in parallel and accelerating flow, in: AIAA, Aerosp. Sci. Meet. Exhib. 34 Th, Reno, NV, 1996.
[18] R.C. Henry, D. Guffond, Fran-atilde, O. Garnier, André, Bouveret, Heat transfer coefficient measurement on iced airfoil in small icing wind tunnel, J. Thermophys. Heat Transf. 14 (2000) 348–354.
[19] M. Vargas, Current experimental basis for modeling ice accretions on swept wings, J. Aircr. 44 (2007) 274–290, https://doi.org/10.2514/1.23323.
[20] T.G. Myers, Extension to the Messinger model for aircraft icing, AIAA J. 39 (2001) 211–218.
[21] G. Fortin, J.-L. Laforte, A. Ilinca, Heat and mass transfer during ice accretion on aircraft wings with an improved roughness model, Int. J. Therm. Sci. 45 (2006) 595–606, https://doi.org/10.1016/j.ijthermalsci.2005.07.006.
[22] N. Dukhan, K.J. De Witt, K.C. Masiulaniec, G.J. Van Fossen, Experimental frossling numbers for ice-roughened NACA 0012 airfoils, J. Aircr. 40 (2003) 1161–1167, https://doi.org/10.2514/2.7205.
[23] L. Tecson, S.T. McClain, Convective enhancement of surfaces with realistic ice roughness distributions, in: 5th AIAA Atmos. Sp. Environ. Conf., American Institute of Aeronautics and Astronautics, 2013. https://doi.org/10.2514/6.2013-3060.
[24] W.B. Wright, User manual for the NASA Glenn ice accretion code LEWICE, National Aeronautics and Space Administration, Glenn Research Center; National Technical Information Service, distributor, Cleveland, Ohio, 1999.
[25] J. Shin, Characteristics of surface roughness associated with leading-edge ice accretion, J. Aircr. 33 (1996) 316–321, https://doi.org/10.2514/3.46940.
[26] M. Vargas, H. Broughton, J.J. Sims, B. Bleeze, V. Gaines, Local and total density measurements in ice shapes, J. Aircr. 44 (2007) 780–789, https://doi.org/10.2514/1.23326.
[27] M.B. Bragg, M.J. Cummings, S. Lee, C.M. Henze, Boundary-layer and heat-transfer measurements on an airfoil with simulated ice roughness, AIAA Pap. 866 (1996) 1–16.
[28] J. Winkler, M. Bragg, Local flowfield about large distributed roughness in the initial ice accretion process, in: 34th Aerosp. Sci. Meet. Exhib., American Institute of Aeronautics and Astronautics, 1996, https://doi.org/10.2514/6.1996-868.
[29] M. Kerho, M. Bragg, Effect of large distributed leading-edge roughness on boundary layer development and transition, in: 13th Appl. Aerodyn. Conf., American Institute of Aeronautics and Astronautics, 1995, https://doi.org/10.2514/6.1995-1803.
[30] J. Bons, K. Christensen, A comparison of real and simulated surface roughness characterizations, in: 37th AIAA Fluid Dyn. Conf. Exhib., 2007, p. 3997.
[31] S.R. Mart, S.T. McClain, L.M. Wright, Turbulent convection from deterministic roughness distributions with varying thermal conductivities, J. Turbomach. 134 (2012) 51030.
[32] L. Tecson, S.T. McClain, Modeling of realistic ice roughness element distributions to characterize convective heat transfer, in: 5th AIAA Atmos. Sp. Environ. Conf., American Institute of Aeronautics and Astronautics, 2013 https://doi.org/10.2514/6.2013-3059.
[33] S. Lee, A. Broeren, H. Addy, R. Sills, E. Pifer, Development of 3D ice accretion measurement method, in: 4th AIAA Atmos. Sp. Environ. Conf., American Institute of Aeronautics and Astronautics, Reston, Virigina, 2012. https://doi.org/10.2514/6.2012-2938.
[34] L. Gao, Y. Liu, W. Zhou, H. Hu, An experimental study on the aerodynamic performance degradation of a wind turbine blade model induced by ice accretion process, Renew. Energy 133 (2019) 663–675, https://doi.org/10.1016/J.RENENE.2018.10.032.
[35] S. Lee, A.P. Broeren, R.E. Kreeger, M.G. Potapczuk, L. Utt, Implementation and validation of 3-D ice accretion measurement methodology, in: 6th AIAA Atmos. Sp. Environ. Conf., American Institute of Aeronautics and Astronautics, 2014. https://doi.org/10.2514/6.2014-2613.
[36] R.J. Hansman, K. Yamaguchi, B. Berkowitz, M. Potapczuk, Modeling of surface roughness effects on glaze ice accretion, J. Thermophys. Heat Transf. 5 (1991) 54–60.
[37] S.T. McClain, R.E. Kreeger, Assessment of Ice Shape Roughness Using a Self-Organizing Map Approach, in: 5th AIAA Atmos. Sp. Environ. Conf., American Institute of Aeronautics and Astronautics, Reston, Virginia, 2013, https://doi.org/10.2514/6.2013-2546.
[38] S.T. McClain, M. Vargas, J.-C. Tsao, A.P. Broeren, S. Lee, Ice Accretion Roughness Measurements and Modeling, Cleveland, OH United States, 2017. https://ntrs.nasa.gov/search.jsp?R=20170008731 (accessed June 13, 2019).
[39] S.M. Soloff, R.J. Adrian, Z.-C. Liu, Distortion compensation for generalized stereoscopic particle image velocimetry, Meas. Sci. Technol. 8 (1997) 1441–1454, https://doi.org/10.1088/0957-0233/8/12/008.
[40] R. Joussot, V. Lago, J.-D. Parisse, Quantification of the effect of surface heating on shock wave modification by a plasma actuator in a low-density supersonic flow over a flat plate, Exp. Fluids 56 (2015) 102, https://doi.org/10.1007/s00348-015-1970-2.
[41] R. Henry, R.J. Hansman, K.S. Breuer, Measurement of heat transfer variation on surface roughness elements using infrared techniques, AIAA Pap. (1994) 94–801.
[42] R. Waldman, H. Hu, High-Speed Imaging to Quantify the Transient Ice Accretion Process on a NACA 0012 Airfoil, in: 53rd AIAA Aerosp. Sci. Meet., 2015.
[43] S. Özgen, M. Canıbek, Ice accretion simulation on multi-element airfoils using extended Messinger model, Heat Mass Transf. 45 (2009) 305–322, https://doi.org/10.1007/s00231-008-0430-4.
[44] K. Zhang, H. Hu, An experimental study on the transient behavior of wind-driven water runback over a flat surface, in: 54th AIAA Aerosp. Sci. Meet., American Institute of Aeronautics and Astronautics, 2016. https://doi.org/10.2514/6.2016-1123.
[45] K. Zhang, T. Wei, H. Hu, An experimental investigation on the surface water transport process over an airfoil by using a digital image projection technique, Exp. Fluids 56 (2015) 1–16, https://doi.org/10.1007/s00348-015-2046-z.
[46] Y. Liu, W.-L. Chen, L.J. Bond, H. Hu, An experimental study on the characteristics of wind-driven surface water film flows by using a multi-transducer ultrasonic pulse-echo technique, Phys. Fluids. 29 (2017) 012102, https://doi.org/10.1063/1.4973398.
[47] D.R. Bilodeau, W.G. Habashi, M. Fossati, G.S. Baruzzi, Eulerian modeling of supercooled large droplet splashing and bouncing, J. Aircr. 52 (2015) 1611–1624, https://doi.org/10.2514/1.C033023.
[48] R.C. Henry, R.J. Hansman, K.S. Breuer, Heat transfer variation on protuberances and surface roughness elements, J. Thermophys. Heat Transf. 9 (1995) 175–180.
[49] J.M. Barros, K.T. Christensen, Observations of turbulent secondary flows in a rough-wall boundary layer, J. Fluid Mech. 748 (2014).